Tungsten Oxide Single Crystal Nanosheets for Enhanced Multichannel Solar Light Harvesting

Junqing Yan, Tuo Wang, Guangjun Wu, Weili Dai, Naijia Guan, Landong Li, and Jinlong Gong**

Semiconductor photocatalysis has attracted significant attention due to its promising application in solar energy conversion, since the discovery of water photolysis on a TiO_2 photoanode in the 1970s.[1] TiO_2 is the initial semiconductor photocatalyst investigated and nowadays it is still the most studied one due to its own advantages. However, TiO_2 is a type of wide bandgap semiconductor and it only adsorbs UV light, which greatly limits its practical applications.[2,3] In addition to extensive researches on reducing the bandgap of TiO_2 for visible light response,[4–8] alternative semiconductors with intrinsic narrow bandgaps are being explored.[9,10]

Tungsten trioxide, known as a nontoxic and photostable n-type semiconductor with a bandgap of ≈2.6 eV, can absorb a significant part of visible light and, therefore, becomes a compelling photocatalyst for solar light harvesting.[11–16] Generally, WO_3 is unable to reduce water to hydrogen because of the insufficient conduction band level for this reaction, while it shows very high activity for water oxidation to oxygen in the presence of a suitable electron acceptor, which can be viewed as a crucial step in artificial photosynthesis.[17] Thereupon, in the past decades, persistent efforts have been made to improve the photocatalytic activity of WO_3, especially in water oxidation, and different strategies have been proposed.[15,18–24]

Nanostructuring is a promising strategy to improve the photocatalytic efficiency of semiconductors.[25,26] Nanocrystalline WO_3 film,[11] mesoporous WO_3 thin film,[12] and hierarchical WO_3 hollow shells[14] have been claimed to exhibit higher photocatalytic activity than bulk WO_3 probably due to their larger surface area and enhanced light scattering. Among all the nanostructured photocatalysts, 2D materials, i.e., nanosheets, receive special attention.[27] Due to the gradient in the potentials of different facets, the photogenerated electrons and holes are driven to the different facets and a p–n junction can be expected at the nanosheet junctions, which accordingly greatly promote the charge-carrier separation. In case of WO_3 nanosheets, remarkable photocatalytic activity one order of magnitude higher than bulk WO_3 powders have been achieved,[20,21] illustrating the great potential of nanosheet construction in promoting the photocatalytic activity.

Introduction of oxygen vacancies to the surface of semiconductors is another promising strategy to improve their photocatalytic efficiency. An elegant example is the disorder-engineered TiO_2 nanocrystals, i.e., hydrogenated TiO_2 nanocrystals, which exhibit remarkable activity in both photo-oxidation and photoreduction reactions.[28] Further work indicates that the introduction of a high density of oxygen vacancies can greatly increase the donor density of TiO_2, and, therefore, can promote the charge-carrier separation, which finally results in the enhancement in photocurrent response and photocatalytic activity.[29] With similar hydrogenation treatments on WO_3, greatly promoted photocurrent responses[22] and photocatalytic activity for water oxidation[23] have been achieved.

In the past decade, surface plasmon resonance on certain conducting metals, e.g., Au and Ag, has been successfully applied in photocatalysis.[30,31] It provides a unique pathway for solar light harvesting, and when combined with semiconductors, the localized surface plasmon resonance (LSPR) can improve the efficiency of charge-carrier separation. For example, modification of semiconductor WO_3 with Ag[24] and Au[32] can enhance the photocurrent and photocatalytic activity, respectively. Recently, transition-metal oxides are recognized as interesting candidates for LSPR hosts, originated from their outer-d valence electrons. Plasmonic molybdenum oxide nanosheets were synthesized and such plasmonic semiconductor nanostructures exhibited enhanced photocatalytic activity under visible light.[33] Particularly, tunable plasmon resonances in the visible range have been recently reported for substoichiometry molybdenum oxide nanoflakes with controlled doping levels and the lateral dimensions of flakes.[34] Tungsten oxides nanocrystals with tunable LSPR have also been successfully prepared;[35] however, the effects of LSPR on their solar light harvesting properties are not investigated yet.

Despite the current achievements on the strategies to promote the photocatalytic activity, WO_3-based semiconductors with adequate activity under visible or solar light are still being explored. Inspired by the pioneer work, herein, we will report the fabrication of tungsten oxide single crystal nanosheets with abundant surface oxygen vacancies as robust semiconductor photocatalysts for solar light harvesting. The theory for catalyst design is that the combination of different strategies, i.e.,

J. Yan, Dr. T. Wang, Dr. G. Wu, Dr. W. Dai, Prof. N. Guan, Prof. L. Li, Prof. J. Gong
Collaborative Innovation Center of Chemical Science and Engineering
Tianjin 300072, P.R. China
E-mail: lild@nankai.edu.cn; jlgong@tju.edu.cn
J. Yan, Dr. G. Wu, Dr. W. Dai, Prof. N. Guan, Prof. L. Li
Key Laboratory of Advanced Energy Materials Chemistry of the Ministry of Education
College of Chemistry
Nankai University
Tianjin 300071, P.R. China
Dr. T. Wang, Prof. J. Gong
Key Laboratory for Green Chemical Technology of Ministry of Education
School of Chemical Engineering and Technology
Tianjin University
Tianjin 300072, P.R. China

DOI: 10.1002/adma.201404792

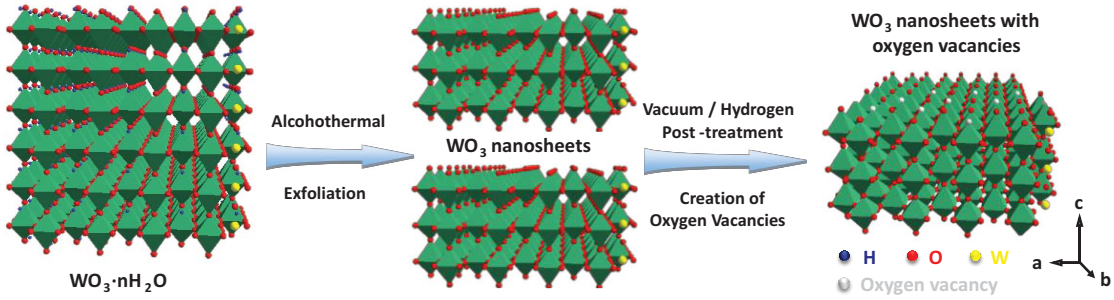

Figure 1. Schematic illustration describing the formation of tungsten oxide single crystal nanosheets.

2D structure construction, the introduction of surface oxygen vacancies, and the creation of LSPR, can promote the light harvesting performance of WO_3 through accumulative and synergistic effects.

Experimentally, tungsten oxide single crystal nanosheets were prepared from tungstic acid via a two-step post-treatment procedure, consisting the exfoliation of layered tungstic acid to tungsten oxide nanosheets and then the introduction of oxygen vacancies, as illustrated in **Figure 1**. First, tungstic acid was hydrothermally synthesized from sodium tungstate and oxalic acid (see Supporting Information for details). X-ray diffraction (XRD) pattern of as-synthesized tungstic acid shows a dominant orthorhombic structure (JCPDS 18–1418, Figure S1, Supporting Information) and the scanning electron microscopy (SEM) image indicates the nanoplate morphology with an average thickness of ≈50 nm (Figure S2, Supporting Information) For the exfoliation of layered tungstic acid into tungsten oxide nanosheets, a most simple and environmental-benign alcohothermal strategy is developed in the present study (see Supporting Information for details). After air annealing, the tungsten oxide nanosheets are finally treated in vacuum or hydrogen to derive the tungsten oxide nanosheets with oxygen vacancies, i.e., WO_{3-x}-VT and WO_{3-x}-HT, respectively.

The WO_3 nanosheets after annealing appear as yellowish powders, which turn olive drab with the introduction of oxygen vacancies (Figure S3, Supporting Information). The diameter of WO_3 nanosheets is in the micrometer level and the average thickness is 15–20 nm, as observed in the SEM images (**Figure 2**). We have performed atomic force microscopy (AFM) analysis on WO_3 nanosheets after annealing and their thickness is determined to be 8–20 nm (Figure S4, Supporting Information). Most of the sheets have a fundamental thickness of 2.1 nm, approximate three layers of the monoclinic WO_3 unit cells.[36] The introduction of oxygen vacancies does not bring about significant changes in the nanosheets morphology. Transmission electron microscopy (TEM) observations also confirm

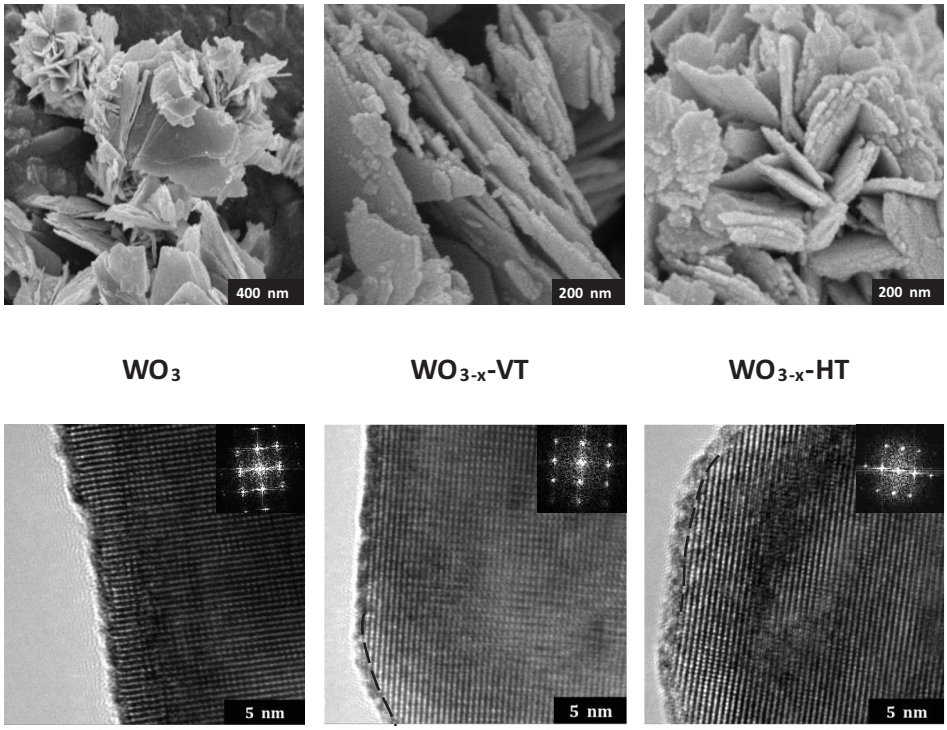

Figure 2. SEM and HRTEM images of WO_3, WO_{3-x}-VT, and WO_{3-x}-HT nanosheets.

the morphology of nanosheets, which appear as aggregates of nanoflowers (Figure S5, Supporting Information). Clear lattice fringes could be observed in the high-resolution transmission electron microscopy (HRTEM) images of nanosheets (Figure 2), revealing their high crystallinity. As depicted from the corresponding fast fourier transform (FFT) images, (200) and (020) atomic planes with angle of 90° could be clearly identified, match well with the WO_3 monoclinic phase of single crystal structure. It has been reported that vacuum or hydrogen treatment can induce the surface disorder of oxides.[27,37] In the present work, similar circumstances happen to WO_3 nanosheets during post-treatments, where a surface disorder layer of ≈1 nm could be observed in WO_{3-x}-VT (as marked in the HRTEM images).

The structure of tungsten oxide nanosheets is extensively investigated via various spectroscopic techniques. The XRD patterns of the tungsten oxide nanosheets under study show the similar monoclinic structure (JCPDS 20–1324) and the clear diffraction peaks indicate the high crystallinity of the samples (**Figure 3**a). While in the enlarged view of XRD patterns in the region of $2\theta = 22°–26°$ (Figure S6, Supporting Information), a slight shift of (020) peak of pristine WO_3 nanosheets towards a higher angle could be observed after hydrogen or vacuum treatment. It is known that with the introduction of oxygen or other cationic vacancies with smaller ionic radius,[38] the interplanar spacing d becomes smaller, which is then reflected as the higher 2θ value of typical diffraction peak in XRD pattern. On the contrary, the thickness of tungsten oxide nanosheets along the *c*-axis is calculated, according to Debye equation, to be ≈16 nm, consistent with electron microscopy observations.

Raman spectroscopy is further employed to investigate the crystalline structure of as-obtained products and to illustrate the formation of surface oxygen vacancies. The Raman spectrum of pristine WO_3 nanosheets is dominated by three major vibration bands at 270, 715, and 805 cm^{-1}, assignable to the bending vibration of δ(O–W–O) and the stretching vibration of ν(W–O–W) of monoclinic phase, respectively.[39] After treatment in vacuum or hydrogen, these vibration bands are well preserved but the W^{6+}–O stretching band at 715 cm^{-1} slightly shifts to a low wavelength of 705 cm^{-1}. Meanwhile, in particular, a new broad band at ≈635 cm^{-1} appears for WO_{3-x}-VT and WO_{3-x}-HT nanosheets (Figure 3b), which has been reported to originate from the Ag phonons of the $WO_3(H_2O)_x$ lattice.[40,41] With the introduction of oxygen vacancies, H_2O tends to adsorb on the oxygen vacancies in WO_3 and form $WO_3(H_2O)_x$ structure.

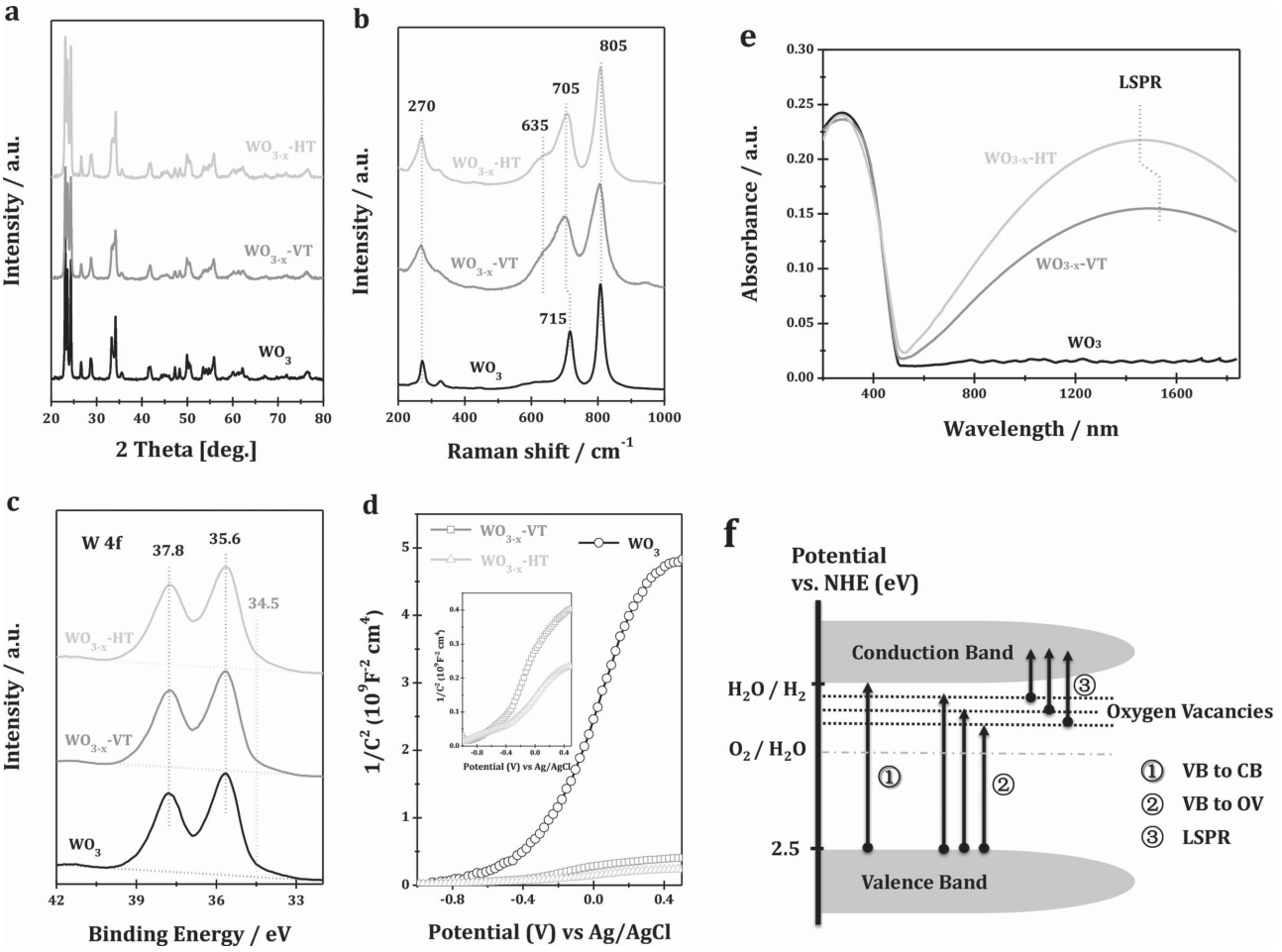

Figure 3. a) XRD patterns, b) Raman spectra, c) W 4f XPS, d) Mott–Schottky plots, e) UV–vis -NIR spectra, and f) band level arrangements of tungsten oxide nanosheets with oxygen vacancies.

Table 1. Physico-chemical properties of tungsten oxide nanosheets under study.

Sample	Crystalline phase	BET [$m^2\ g^{-1}$]	Apparent color	LSPR peak [nm]	Free-carrier density [cm^{-3}]	
WO_3	Monoclinic	133	Yellowish	–	8.6×10^{19} [a]	–
WO_{3-x}-VT	Monoclinic	131	Olive drab	1450	1.7×10^{21} [a]	2.0×10^{21} [b]
WO_{3-x}-HT	Monoclinic	129	Olive drab	1520	2.3×10^{21} [a]	2.5×10^{21} [b]

[a] Calculated from Mott–Schottky plots: $N_d = \left(\frac{2}{e_0 \varepsilon_0 \varepsilon}\right)\left[d\left(\frac{1}{c^2}\right)/dv\right]^{-1}$; [b] Calculated from UV–vis -NIR spectra by using the Drude model: $\omega_p = \sqrt{\frac{N_e e^2}{\varepsilon_0 m_e}}$.

Figure 3c shows the high resolution W 4*f* X-ray photoelectron spectra (XPS) of tungsten oxide nanosheets. For all samples, binding energy values at 35.6 and 37.8 eV are observed, which are assigned to $4f_{7/2}$ and $4f_{5/2}$ of W^{6+} in WO_3, respectively.[22,23] The existence of W^{5+} with binding energy values at 34.5 and 36.7 eV could not be distinguished in the spectra due to the overlap with the strong signals from W^{6+}. Treatment in hydrogen or vacuum does not bring about significant changes in the W 4*f* or O 1s XPS (Figure S7, Supporting Information), indicating the similar structure of tungsten oxide nanosheets investigated.

The flat-band potential of tungsten oxide nanosheets is measured using the electrochemical method and the Mott–Schottky plots are shown in Figure 3d. The Mott–Schottky plots of all the samples show a positive slope, which is typical for n-type semiconductors. WO_{3-x}-VT and WO_{3-x}-HT show much smaller slopes of Mott–Schottky plots compared to the pristine WO_3 nanosheets, revealing the enhanced carrier densities after treatments.[22] The donor density could be calculated from the slopes in the Mott–Schottky plots according to the below equation

$$N_d = \left(\frac{2}{e_0 \varepsilon_0 \varepsilon}\right)\left[d\left(\frac{1}{c^2}\right)/dv\right]^{-1}$$

where N_d is the donor density, e_0 is the electron charge, ε_0 is the permittivity of vacuum, ε is the dielectric constant of WO_3 ($\varepsilon = 20$), and V is the applied bias at the electrode. The dramatically enhanced donor densities of WO_{3-x}-VT (1.7×10^{21} cm^{-3}) and WO_{3-x}-HT (2.3×10^{21} cm^{-3}), comparing with the pristine WO_3 (8.6×10^{19} cm^{-3}), should be attributed to the introduction of oxygen vacancies, which are known to be electron donors.[42] We also performed Hall measurements on the free carrier densities and values of 5.7×10^{19}, 1.2×10^{21}, and 1.9×10^{21} cm^{-3} were obtained for WO_3, WO_{3-x}-VT, and WO_{3-x}-HT, respectively. The values are slightly lower than those calculated from Mott–Schottky plots, but a similar trend is clearly observed, further confirming the dramatically enhanced free carrier densities upon the introduction of oxygen vacancies.

On the basis of the electron microscopic observations and the spectroscopic characterizations, it is clearly seen that WO_3 single crystal nanosheets are successfully obtained from the exfoliation of layered tungstic acid. Post-treatment in vacuum or hydrogen under mild conditions does not bring out significant changes in the bulk structure of WO_3 nanosheets but does induce a great amount of oxygen vacancies, which dominantly locate at the outer surface of nanosheets as a disorder layer. With the above-mentioned information on the structure of tungsten oxide nanosheets, we further examined their optical properties that might be influenced by the structural configurations. As shown in the diffuse reflectance UV–vis-NIR spectra in Figure 3e, all samples show similar intrinsic absorption up to ≈480 nm, consistent with the indirect bandgap absorption edge of WO_3 at ≈2.6 eV. For WO_{3-x}-VT and WO_{3-x}-HT, optical absorption beyond the band edge, e.g., in 480–700 nm region, could be observed, which should be due to the new discrete energy bands below the conduction band created by the introduction of anionic vacancies.[29,43] Moreover, light absorption in the near-infrared region, with intensity comparable with the bandgap absorption, could be observed for tungsten oxygen nanosheets with oxygen vacancies, i.e., WO_{3-x}-VT and WO_{3-x}-HT. According to the results from Mott–Schottky plots and Hall effect measurements, a large amount of free conduction band electrons, with free-carrier density of over 10^{21} cm^{-3}, can be identified and the collective oscillations of surface free carriers (electron for n-type semiconductor WO_3) can induce the surface plasmon resonance.[31,35] Typically, LSPR peaks centered at ≈1520 and 1450 nm are observed for WO_{3-x}-VT and WO_{3-x}-HT, respectively. We further calculated the free-carrier density from LSPR peak according to the Drude model[35]

$$\omega_p = \sqrt{\frac{N_e e^2}{\varepsilon_0 m_e}} \quad (2)$$

where ω_p is the bulk plasma frequency, e is the elementary charge, ε_0 is the permittivity of free space, and m_e is the effective mass of an electron, and N_e is the charge-carrier density. The charge-carrier densities of WO_{3-x}-VT and WO_{3-x}-HT are determined to be 2.0×10^{21} and 2.5×10^{21} cm^{-3}, respectively, in good agreement with those calculated from Mott–Schottky plots (**Table 1**), confirming the validity of LSPR theory for tungsten oxides employed in this study. It should be mentioned that in contrast to most other nonstoichiometric metal oxides, e.g., TiO_{2-x}, WO_{3-x} is thermodynamically stable under ambient conditions and the quench of oxygen vacancies is reported to occur only upon annealing in air at the temperature higher than 673 K.[22] In this study, the LSPR absorption peak at ≈1520 nm of WO_{3-x}-HT nanosheets caused by the oxygen vacancies remains unchanged after annealing in air at 353 K, while a significant decrease in the LSPR intensity is observed after annealing at 573 K (Figure S8, Supporting Information). According to properties of tungsten oxide nanosheets with oxygen vacancies, the band level arrangements and the separation of photoexcited electron–hole pairs in this type of semiconductor are illustrated in Figure 3f. Theoretically, there are three different channels for solar light harvesting: (1) electrons

excited from valence band top to conduction bottom; (2) electrons excited from valence band top to oxygen vacancies below the conduction band; and (3) electrons excited by LSPR.

The solar light harvesting properties of tungsten oxides nanosheets are examined by means of photocurrent responses and photocatalytic evaluation. We first measured the photocurrent response in a three-electrode electrochemical cell with Ag/AgCl as the reference electrode and Pt wire as the counter electrode (see Supporting Information for details). The photocurrent responses for all samples under dark are very low, while obvious current responses could be discerned from 0.2 to 1.0 eV (vs Ag/AgCl) under full-spectrum light (**Figure 4**a). WO_{3-x}-HT shows the highest photocurrent density, followed by WO_{3-x}-VT and then pristine WO_3 nanosheets, indicating that WO_{3-x}-HT should be better semiconductor material for solar light harvesting. For a better understanding on the light harvesting by tungsten oxide nanosheets, the photocurrent responses under different illumination conditions are examined. Under UV (Figure 4b) or visible light (Figure 4c), WO_{3-x}-HT nanosheets show the highest photocurrent density, followed by WO_{3-x}-VT and then pristine WO_3 nanosheets. The enhanced photocurrent responses of WO_{3-x}-HT and WO_{3-x}-VT as compared with WO_3 nanosheets should be related to the oxygen vacancies introduced during post-treatments. As revealed by photoluminescence (PL) analysis (corresponding discussion and Figure S9, Supporting Information), the recombination of photogenerated electron-hole pairs is effectively suppressed upon the introduction of oxygen vacancies, which accordingly results in higher photocurrent responses. The higher conductive ability of WO_{3-x}-HT and WO_{3-x}-VT samples, as revealed by the dark *I–V* scans in Figure S10 (Supporting Information), may also contribute to their higher photocurrent responses.[29] Moreover, WO_{3-x}-VT and WO_{3-x}-HT nanosheets also show noticeable photocurrent responses under near-infrared illumination, in great contrast to pristine WO_3 nanosheets (Figure 4d). The observed photocurrent responses under near-infrared illumination should come from LSPR induced by the abundant oxygen vacancies (vide supra). On the basis of photocurrent responses under different illumination conditions, we could come to the conclusion that the introduction of surface oxygen vacancies to

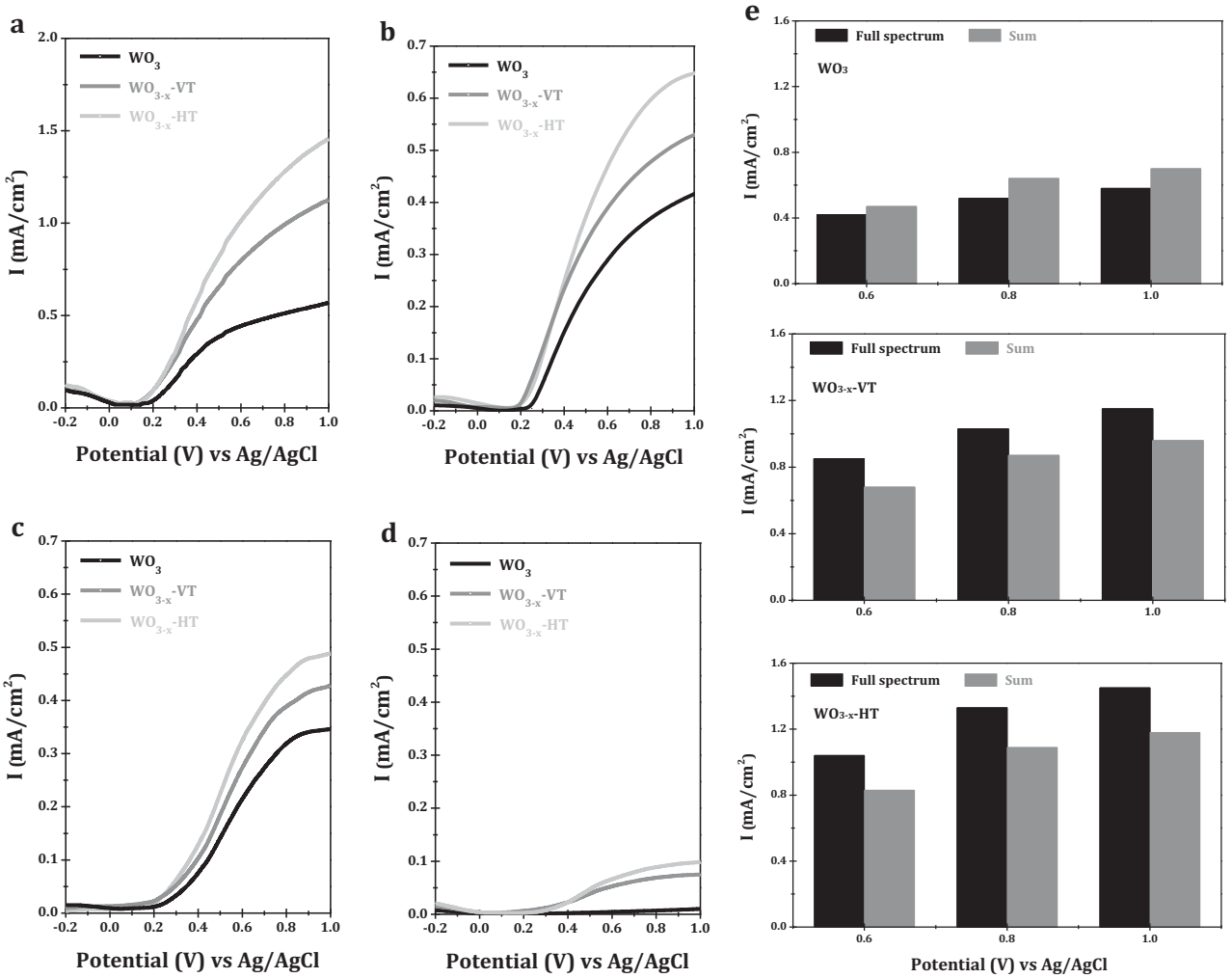

Figure 4. Photocurrent response of WO_3, WO_{3-x}-VT, and WO_{3-x}-HT nanosheets under the illumination of a) full-spectrum UV–vis -NIR light (300–2000 nm), b) UV light (300–400 nm), c) visible light (400–780 nm), d) NIR light (780–2000 nm), and e) the comparison between full-spectrum and the sum of individual UV, vis, and NIR light.

tungsten oxide nanosheets can not only promote UV and visible light harvesting but also create near-infrared harvesting, attaining the so-called multichannel solar light harvesting. Under the illumination of full-spectrum light, the photocurrent values observed for WO_3 nanosheets is slightly lower (≈10%) than the sum of values under individual UV, visible and near-infrared illumination (Figure 4e), which could be considered as common knowledge due to the mutual influence between protons with different energies. However, in contrast to the case of WO_3 nanosheets, the observed photocurrent values for WO_{3-x}-VT or WO_{3-x}-HT under full-spectrum light are distinctly higher (20%–30%) than the sum of values under individual UV, visible and near-infrared illumination at all bias voltages investigated (Figure 4e). Obviously, the synergetic promotion of photocurrent response under full-spectrum light exists in tungsten oxide nanosheets with oxygen vacancies, i.e., WO_{3-x}-VT and WO_{3-x}-HT. One origination of the synergetic effects might come from the LSPR of samples, which may enhance the local electric field of tungsten oxides and accordingly promote the charge-carrier separation.[44,45] Another origination might come from the electron affinity of oxygen vacancies, which acts like cocatalysts on semiconductors and promotes the charge-carrier separation.[46]

The light harvesting properties of tungsten oxides nanosheets (without cocatalyst) are further examined in the reaction of photocatalytic oxygen evolution from water oxidation ($NaIO_3$ as sacrificial reagent, see Supporting Information for details). Under UV or visible light (**Figure 5**a), WO_{3-x}-HT exhibits the highest mass specific activity, followed by WO_{3-x}-VT and then WO_3. The trend is consistent with the experimental observations in photocurrent responses (Figure 4b,c). Under near-infrared light, no oxygen evolution is observed over all samples although photocurrent responses could be detected for WO_{3-x}-VT and WO_{3-x}-HT (Figure 4d). This should be due to the fact that the holes created by LSPR are insufficient to oxidize water to oxygen. Under simulated solar light, i.e., Air Mass 1.5, WO_{3-x}-HT exhibits the highest mass specific activity of 1593 μmol (h gcat)$^{-1}$, ≈20% higher than 1346 μmol (h gcat)$^{-1}$ of WO_{3-x}-VT and over 2.5 times higher than 606 μmol (h gcat)$^{-1}$ of pristine WO_3 nanosheets (reference bulk WO_3 shows very low activity of 53 μmol (h gcat)$^{-1}$, this value increases to 73 and 89 μmol (h gcat)$^{-1}$ upon vacuum and hydrogen treatments, respectively). To our knowledge, the oxygen evolution rate achieved on WO_{3-x}-HT is much greater than most WO_3 semiconductors reported under comparable conditions.[20,23] For a more objective comparison between the photocatalytic efficiencies for oxygen evolution under different illumination, the apparent quantum yield (QY) was calculated. Typically, QYs of 14.8%, 11.6%, 9.3%, 1.5%, and 0.2% are obtained on WO_{3-x}-HT nanosheets under monochromatic light at λ = 350, 405, 420, 475, and 550 nm, respectively, which agrees well with the light absorption ability (Figure 3e). We further investigated the effects of additional near-infrared light on the photocatalytic oxygen evolution over WO_{3-x}-HT under different monochromatic light and the results are shown Figure 5b. It is clearly seen that additional near-infrared light could promote oxygen evolution to some extent, independent on the wavelength of the monochromatic light employed. Considering that near-infrared light itself could not induce oxygen evolution (Figure 5a), the promotion of oxygen evolution should be due to the enhanced charge-carrier separation by LSPR, similar to the case in photocurrent responses (vide supra). Moreover, it should be mentioned that the WO_3 nanosheets, coupled with certain cocatalysts, might be potential semiconductor photocatalysts for overall water splitting since their conduction band bottom is more negative than the reduction potential of H_2O/H_2 and their valence band top is more positive than the oxidation potential of O_2/H_2O.

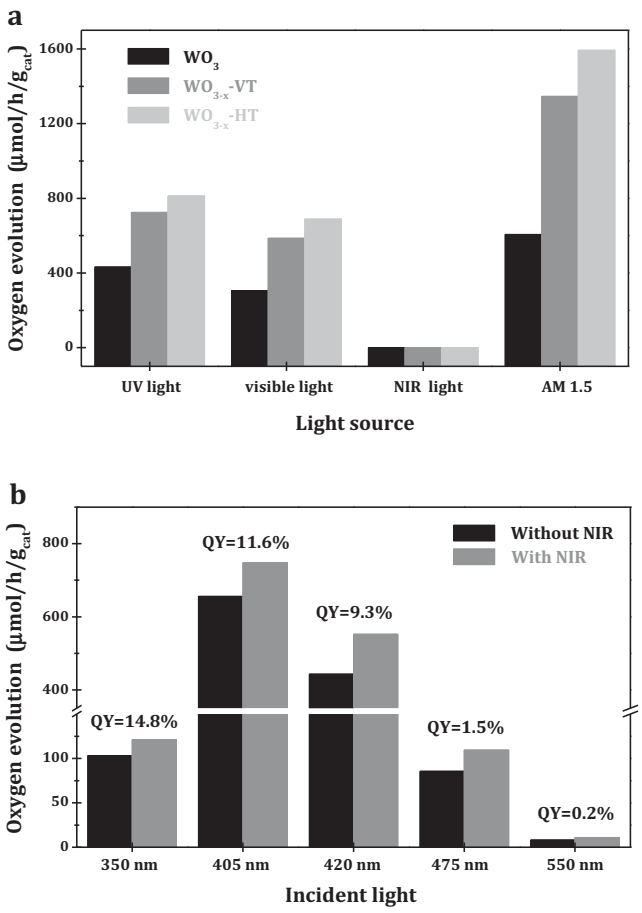

Figure 5. a) Photocatalytic oxygen evolution over WO_3, WO_{3-x}-VT, and WO_{3-x}-HT nanosheets under different illumination conditions; b) Promotion of photocatalytic oxygen evolution over WO_{3-x}-HT under monochromatic light at λ = 350, 405, 420, 475, and 550 nm by the introduction of near-infrared light (780–2000 nm).

In summary, substoichiometric tungsten oxide single crystal nanosheets were successfully prepared via the exfoliation of layered tungstic acid to tungsten oxide nanosheets and subsequent introduction of oxygen vacancies. The as-prepared substoichiometric tungsten oxide nanosheets showed dramatically enhanced performance in both photocurrent responses and photocatalytic water oxidation. The introduction of oxygen vacancies to pristine tungsten oxide nanosheets can induce the surface plasmon resonance, which not only creates the light harvesting via LSPR in the near-infrared region but also promotes the light harvesting in the ultraviolet and visible region. Our experimental observations clearly reveal that under delicate design, the combination of different strategies can promote

the light harvesting performance of pristine semiconductors through accumulative and synergistic effects.

We hope that the theory for material design developed in the present study can be simply expanded to the fabrication of other robust semiconductor photocatalyst systems. The concept of multichannel solar light harvesting should shed a light for practical solar energy utilization.

Supporting Information

Supporting Information is available from the Wiley Online Library or from the author.

Acknowledgements

J.Y. and T.W. equally contributed to this work. We acknowledge the National Science Foundation of China (Grant Nos. U1463205, 21222604, and 51302185), the Specialized Research Fund for the Doctoral Program of Higher Education (No. 20120032110024), the Scientific Research Foundation for the Returned Overseas Chinese Scholars (MoE), the Ministry of Education of China (Grant Nos. IRT-13R30 and IRT-13022), and the Program of Introducing Talents of Discipline to Universities (Grant Nos. B06006 and B12015) for financial support.

Received: October 16, 2014
Revised: December 7, 2014
Published online: January 12, 2015

[1] A. Fujishima, K. Honda, *Nature* **1972**, *238*, 37.
[2] X. B. Chen, S. S. Mao, *Chem. Rev.* **2007**, *107*, 289.
[3] Y. Ma, X. Wang, Y. Jia, X. Chen, H. Han, C. Li, *Chem. Rev.* **2014**, *114*, 9987.
[4] R. Asahi, T. Morikawa, T. Ohwaki, K. Aoki, Y. Taga, *Science* **2001**, *293*, 269.
[5] S. U. Khan, M. Al-Shahry, W. B. Ingler, *Science* **2002**, *297*, 224.
[6] I. Justicia, P. Ordejón, G. Canto, J. L. Mozos, J. Fraxedas, G. A. Battiston, R. Gerbasi, A. Figueras, *Adv. Mater.* **2002**, *14*, 1399.
[7] J. G. Tao, T. Luttrell, M. Batzill, *Nat. Chem.* **2011**, *3*, 296.
[8] X. B. Chen, C. Burda, *J. Am. Chem. Soc.* **2008**, *130*, 5018.
[9] M. D. Hernández-Alonso, F. Fresno, S. Suáreza, J. M. Coronado, *Energy Environ. Sci.* **2009**, *2*, 1231.
[10] A. Kudo, Y. Miseki, *Chem. Soc. Rev.* **2009**, *38*, 253.
[11] C. Santato, M. Ulmann, J. Augustynski, *Adv. Mater.* **2001**, *13*, 511.
[12] S. H. Baeck, K. S. Choi, T. F. Jaramillo, G. D. Stucky, E. W. McFaland, *Adv. Mater.* **2003**, *15*, 1269.
[13] R. Abe, H. Takami, N. Murakami, B. Ohtani, *J. Am. Chem. Soc.* **2008**, *130*, 7780.
[14] D. Chen, J. H. Ye, *Adv. Funct. Mater.* **2008**, *18*, 1922.
[15] S. S. K. Ma, K. Maeda, R. Abe, K. Domen, *Energy Environ. Sci.* **2012**, *5*, 8390.
[16] H. Zheng, J. Z. Ou, M. S. Strano, R. B. Kaner, A. Mitchell, K. Kalantar-zadeh, *Adv. Funct. Mater.* **2011**, *21*, 2175.
[17] J. R. Darwent, A. Mills, *J. Chem. Soc., Faraday Trans.* **1982**, *78*, 359.
[18] Y. Miseki, H. Kusama, H. Sugihara, K. Sayama, *J. Phys. Chem. Lett.* **2010**, *1*, 1196.
[19] F. Wang, C. D. Valentin, G. Pacchioni, *J. Phys. Chem. C* **2012**, *116*, 8901.
[20] D. L. Chen, L. Gao, A. Yasumori, K. Kuroda, Y. Sugahara, *Small* **2008**, *4*, 1813.
[21] X. Y. Chen, Y. Zhou, Q. Liu, Z. D. Li, J. G. Liu, Z. G. Zou, *ACS Appl. Mater. Interfaces* **2012**, *4*, 3372.
[22] G. Wang, Y. Ling, H. Wang, X. Yang, C. Wang, J. Z. Zhang, Y. Li, *Energy Environ. Sci.* **2012**, *5*, 6180.
[23] G. Liu, J. F. Han, X. Zhou, L. Huang, F. X. Zhang, X. L. Wang, C. M. Ding, X. J. Zheng, H. X. Han, C. Li, *J. Catal.* **2013**, *307*, 148.
[24] R. Solarska, A. Krolikowska, J. Augustynski, *Angew. Chem Int. Ed.* **2011**, *49*, 7980.
[25] F. E. Osterloh, *Chem. Soc. Rev.* **2013**, *42*, 2294.
[26] P. F. Yin, T. Ling, Y. R. Lu, Z. W. Xu, S. Z. Qiao, X. W. Du, *Adv. Mater.* **2014**, DOI: 10.1002/adma.201403947.
[27] S. Ida, T. Ishihara, *J. Phys. Chem. Lett.* **2014**, *5*, 2533.
[28] X. B. Chen, L. Liu, P. Y. Yu, S. S. Mao, *Science* **2011**, *331*, 746.
[29] G. M. Wang, H. Y. Wang, Y. C. Ling, Y. C. Tang, Xu. Y. Yang, R. C. Fitzmorris, C. C. Wang, J. Z. Zhang, Y. Li, *Nano Lett.* **2011**, *11*, 3026.
[30] S. Linic, P. Christopher, D. B. Ingram, *Nat. Mater.* **2011**, *10*, 911.
[31] W. B. Hou, S. B. Cronin, *Adv. Funct. Mater.* **2013**, *23*, 1612.
[32] A. Tanaka, K. Hashimoto, H. Kominami, *J. Am. Chem. Soc.* **2014**, *136*, 586.
[33] H. F. Cheng, T. Kamegawa, K. Mori, H. Yamashita, *Angew. Chem Int. Ed.* **2014**, *53*, 2910.
[34] M. M. Y. A. Alsaif, K. Latham, M. R. Field, D. D. Yao, N. V. Medehkar, G. A. Beane, R. B. Kaner, S. P. Russo, J. Z. Ou, K. Kalantar-zadeh, *Adv. Mater.* **2014**, *26*, 3931.
[35] K. Manthiram, A. P. Alivisatos, *J. Am. Chem. Soc.* **2012**, *134*, 3995.
[36] K. Kalantar-zadeh, A. Vijayaraghavan, M. H. Ham, H. Zheng, M. Breedon, M. S. Strano, *Chem. Mater.* **2010**, *22*, 5660.
[37] C. Y. Yang, Z. Wang, T. Q. Lin, H. Yin, X. J. Lv, D. Y. Wan, T. Xu, C. Zheng, J. H. Lin, F. Q. Huang, X. M. Xie, M. H. Jiang, *J. Am. Chem. Soc.* **2013**, *135*, 17831.
[38] B. Liu, H. M. Chen, C. Liu, S. C. Andrews, C. Hahn, P. D. Yang, *J. Am. Chem. Soc.* **2013**, *135*, 9995.
[39] A. Wolcott, T. R. Kuykendall, W. Chen, S. Chen, J. Z. Zhang, *J. Phys. Chem. B* **2006**, *110*, 25288.
[40] M. F. Daniel, B. Desbat, J. C. Lassegues, R. Garie, *J. Solid State Chem.* **1988**, *73*, 127.
[41] E. Salje, *Acta Cryst. A* **1975**, *31*, 360.
[42] S. K. Deb, *Phys. Rev. B: Condens. Matter Mater. Phys.* **1977**, *16*, 1020.
[43] T. R. Gordon, M. Cargnello, T. Paik, F. Mangolini, R. T. Weber, P. Fornasiero, C. B. Murray, *J. Am. Chem. Soc.* **2012**, *134*, 6751.
[44] K. Awazu, M. Fujimaki, C. Rockstuhl, J. Tominaga, H. Murakami, Y. Ohki, N. Yoshida, T. Watanabe, *J. Am. Chem. Soc.* **2008**, *130*, 1676.
[45] J. Q. Yan, G. J. Wu, N. J. Guan, L. D. Li, *Chem. Commun.* **2013**, *49*, 11767.
[46] J. H. Yang, D. G. Wang, H. X. Han, C. Li, *Acc. Chem. Res.* **2013**, *46*, 1900.